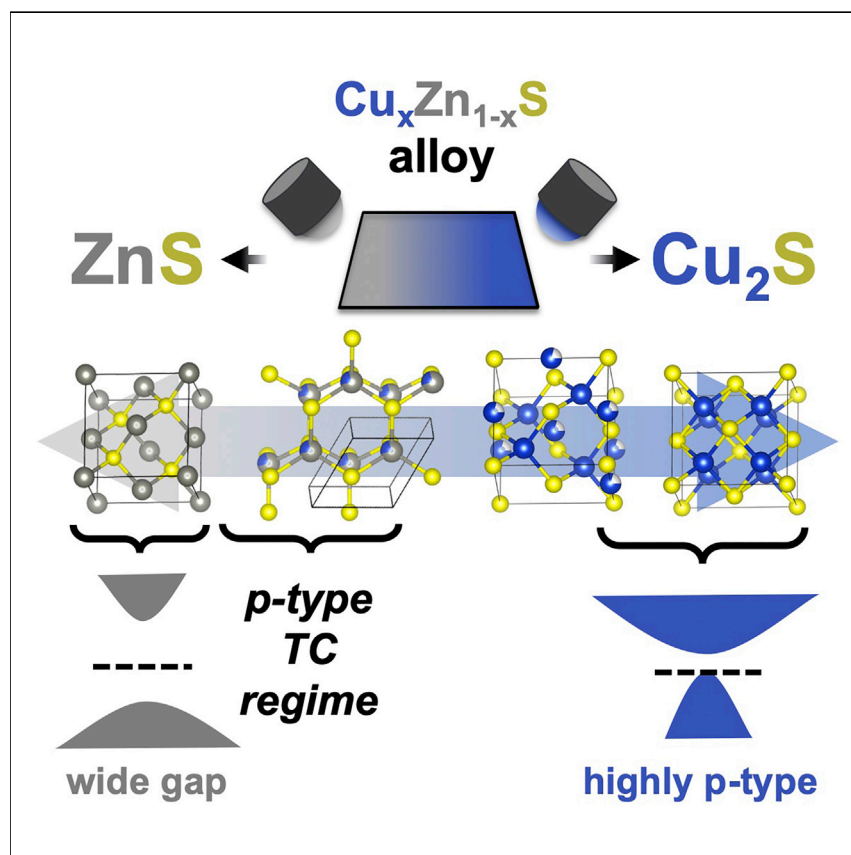


Article

Combinatorial Tuning of Structural and Optoelectronic Properties in $\text{Cu}_x\text{Zn}_{1-x}\text{S}$ 

Developing p-type transparent conductors (TCs) remains an outstanding challenge in optoelectronics and photovoltaics. This study uses combinatorial sputtering and spatially resolved characterization to map the full cation alloy space of $\text{Cu}_x\text{Zn}_{1-x}\text{S}$, a promising p-type TC. Formation of a metastable wurtzite alloy is observed between two cubic endpoints, leading to an electrical conductivity jump and onset of a wide-gap p-type semiconducting regime. These findings motivate further exploration of $\text{Cu}_x\text{Zn}_{1-x}\text{S}$, p-type TC development and continued application of the combinatorial materials discovery approach.

Rachel Woods-Robinson,
Yanbing Han, John S.
Mangum, ..., Apurva Mehta,
Kristin A. Persson, Andriy
Zakutayev

rwoodsrobinson@lbl.gov

HIGHLIGHTS

$\text{Cu}_x\text{Zn}_{1-x}\text{S}$ structure-property relations are mapped across full cation composition space

A metastable wurtzite $\text{Cu}_x\text{Zn}_{1-x}\text{S}$ alloy forms between two cubic binary endpoints

The wurtzite structure correlates with increased p-type conduction and transparency

A p-type transparent region is observed and contextualized with literature reports



3 Understanding

Dependency and conditional studies on material behavior

Woods-Robinson et al., Matter 1, 1–19
November 6, 2019 Published by Elsevier Inc.
<https://doi.org/10.1016/j.matt.2019.06.019>

Article

Combinatorial Tuning of Structural and Optoelectronic Properties in $\text{Cu}_x\text{Zn}_{1-x}\text{S}$

Rachel Woods-Robinson,^{1,2,3,8,*} Yanbing Han,^{1,4} John S. Mangum,⁵ Celeste L. Melamed,^{1,5} Brian P. Gorman,⁵ Apurva Mehta,⁶ Kristin A. Persson,^{3,7} and Andriy Zakutayev¹

SUMMARY

P-type transparent conductors (TCs) are important enabling materials for optoelectronics and photovoltaics, but their performance still lags behind n-type counterparts. Recently, semiconductor $\text{Cu}_x\text{Zn}_{1-x}\text{S}$ has demonstrated potential as a p-type TC, but it remains unclear how properties vary with composition. Here, we investigate $\text{Cu}_x\text{Zn}_{1-x}\text{S}$ across the entire alloy space ($0 \leq x \leq 1$) using combinatorial sputtering and high-throughput characterization. First, we find a metastable wurtzite alloy at an intermediate composition between cubic endpoint compounds, contrasting with solid solutions or cubic composites ($\text{ZnS}:\text{Cu}_y\text{S}$) from the literature. Second, structural transformations correlate with shifts in hole conductivity and absorption; specifically, conductivity increases at the wurtzite phase transformation ($x \approx 0.19$). Third, conductivity and optical transparency are optimized within a "TC regime" of $0.10 < x < 0.40$. This investigation reaffirms $\text{Cu}_x\text{Zn}_{1-x}\text{S}$ as a promising, tunable, multifunctional semiconductor alloy, provides new insight into composition-dependent evolution of structure and properties, and informs future research into device applications.

INTRODUCTION

Achieving a p-type transparent conductor (TC) with properties similar to n-type TCs such as tin-doped indium oxide (ITO) and aluminum-doped zinc oxide (AZO) remains an outstanding challenge in optoelectronic applications, and in particular for photovoltaics.¹ Although n-type TCs are usually oxides, recently there has been an upsurge of interest in non-oxide chalcogenide materials as potential p-type TCs.² Despite their lower gaps and stability challenges, sulfides offer several distinct advantages over oxides that directly address the challenges of achieving p-dopable TCs. First, due to the position of S-3p orbitals, the valence bands of sulfides could have greater hybridization and delocalization than oxides.³ This could lead to lower hole effective masses which could correlate to elevated hole mobilities. Second, the higher position of their valence bands suggests higher p-type dopability than oxides.³ These advantages have been demonstrated in the development of high-performing TC chalcogenides such as self-doped and Zn-doped CuAlS_2 (with one of the highest conductivities of p-type TCs in the literature reported at 250 S cm^{-1}),^{4,5} BaCu_2S_2 ,^{6,7} and Cu_3TaS_4 ,⁸ and mixed anion chalcogenides such as $\text{LaCuO}(\text{S,Se})$ ⁹ and $\text{BaCu}(\text{S,Se,Te})\text{F}$.¹⁰ More recently, several TC chalcogenides have been predicted using high-throughput computational screenings, and remain to be achieved experimentally.^{11,12}

One particularly promising p-type chalcogenide is the ternary compound $\text{Cu}_x\text{Zn}_{1-x}\text{S}$ (also notated Cu-Zn-S , CuZnS , $\text{ZnS}:\text{Cu}_y\text{S}$, and $\text{Cu}_x\text{Zn}_{1-x}\text{S}_{1-\delta}$). $\text{Cu}_x\text{Zn}_{1-x}\text{S}$ combines

Progress and Potential

Advancing renewable energy technologies requires development of new materials. One missing link in photovoltaic (PV) solar cells are semiconductors that are optically transparent and electrically conductive, a combination of properties that is rare in nature. In particular, so-called "p-type" transparent conductors (TCs) could enable more efficient charge extraction in PV, so extensive research has ensued to find suitable p-type TCs.

This work elucidates the evolution of crystal structure and physical properties across a non-oxide p-type TC system formed by alloying transparent ZnS with p-type conductive Cu_yS . The method of selecting two binary endpoints and tailoring their properties is a promising pathway to discover and optimize new p-type TCs. By coupling combinatorial experiments with theoretical calculations, we demonstrate a high-throughput approach to design properties of PV materials.

the properties of a wide-gap insulator, ZnS, with an absorbing p-type semiconductor, Cu_yS . Zinc sulfide typically crystallizes in a low-temperature zinc blende (ZB) ZnS phase ($F\bar{4}3m$ space group, band gap $E_g \approx 3.7$ eV) or a high-temperature wurtzite (WZ) ZnS phase in a variety of polytype stackings ($P6_3mc$, $E_g \approx 3.9$ eV).¹³ Copper sulfide crystallizes in a variety of stoichiometries and nominal oxidation states, most commonly covellite CuS (space group $Cmcm$, $E_g \approx 0.6$ – 1 eV) or chalcocite Cu_2S (space group $P2_1/c$, $E_g \approx 1.2$ – 2 eV), although compounds Cu_yS ($y = 1.6, 1.8, \text{etc.}$) with mixed nominal Cu oxidation states are also common, so we will use the notation Cu_yS herein. At dilute dopings ($x < 0.005$), Cu-doped ZnS nanoparticles and films have been studied as electrochromic materials and photocatalysts,^{14–16} and at higher concentrations alloys have been explored.

$\text{Cu}_x\text{Zn}_{1-x}\text{S}$ was first demonstrated as a p-type TC in 2011 using electrochemical deposition, although previous studies of doping ZnS with Cu had alluded to its application.^{17,18} The $\text{Cu}_x\text{Zn}_{1-x}\text{S}$ p-type TC alloy gained prominence in 2012, when pulsed laser deposition (PLD) yielded thin films with simultaneous hole conductivities up to 56 S cm^{-1} and elevated optical transparencies.¹⁹ Additional studies demonstrated synthesis at ambient temperature using PLD can retain crystallinity, high transparencies, and similar conductivities,²⁰ and that annealing can further increase conductivity.²¹ A significant step was development of a facile, low-temperature chemical bath deposition (CBD) approach, yielding ZnS: Cu_yS composites with conductivities on the order of 10^3 S cm^{-1} , albeit with drops in transparency.²² Subsequently, this compound has been synthesized via various chemical and physical methods, e.g., sol gel,²³ spray pyrolysis,^{24,25} atomic layer deposition (ALD),^{26,27} and sputtering,^{28,29} among others (see Table S1). We emphasize that remarkable properties and crystalline films have been achieved even at low deposition temperatures; this is particularly advantageous to applications in optoelectronic devices with low thermal budgets, such as CdTe and perovskite photovoltaics (PV).^{30,31} Accordingly, $\text{Cu}_x\text{Zn}_{1-x}\text{S}$ films of various crystallinity and microstructure have been recently demonstrated as, e.g., a transparent electrode in $\text{np}^+\text{:Si}$ PV devices with a demonstrated maximum open-circuit voltage of 535 mV,²² a back contact on CdTe solar cells to enable bifacial PV,³² a top contact on perovskite PV,³³ and a junction partner in self-powered UV photodetectors,^{34,35} among other applications.

As this material space gains prominence in the photovoltaic community and beyond, it is important to understand the structural driving forces of high conductivity and stability. Among the previously mentioned studies, this compound tends to either (1) phase segregate into a nanocomposite material (ZnS and Cu_yS), usually with chemical synthesis methods, (2) form a heterostructural, heterovalent alloy to varying degrees, usually with physical deposition methods, or (3) some combination of the first two (see Perspective). However, it is still not fully understood what exactly is responsible for elevated conductivity in this material: a conducting network of semimetallic Cu_yS or metallic Cu phases, doping of Cu^{+1} cations into ZnS, realization of a unique heterovalent ternary alloy, or some combination of these effects?³⁶ In particular, why can high performance be achieved at such low synthesis temperatures? Additionally, to our knowledge there has been no exploration yet of structure-property relations across full cation composition space, which could provide insight into the compound's formation conditions and thermodynamic stability.

In this study, we investigate the $\text{Cu}_x\text{Zn}_{1-x}\text{S}_{1-\delta}$ phase space using combinatorial sputtering at low deposition temperature, as depicted in Figure 1A. We focus on the role of Cu concentration x across its entire composition space ($0 \leq x \leq 1$), since the tuning of cations is primarily responsible for the shift

¹Materials Science Center, National Renewable Energy Laboratory, Golden, CO 80401, USA

²Applied Science and Technology Graduate Group, University of California Berkeley, Berkeley, CA 94720, USA

³Energy Technologies Area, Lawrence Berkeley National Laboratory, Berkeley, CA 94720, USA

⁴Department of Materials Science, Fudan University, Shanghai 200433, China

⁵Metallurgical and Materials Engineering, Colorado School of Mines, Golden, CO 80401, USA

⁶Stanford Synchrotron Radiation Laboratory, SLAC National Laboratory, Menlo Park, CA 94025, USA

⁷Department of Materials Science and Engineering, University of California, Berkeley, CA 94720, USA

⁸Lead Contact

*Correspondence: rwoodsrobinson@lbl.gov
<https://doi.org/10.1016/j.matt.2019.06.019>

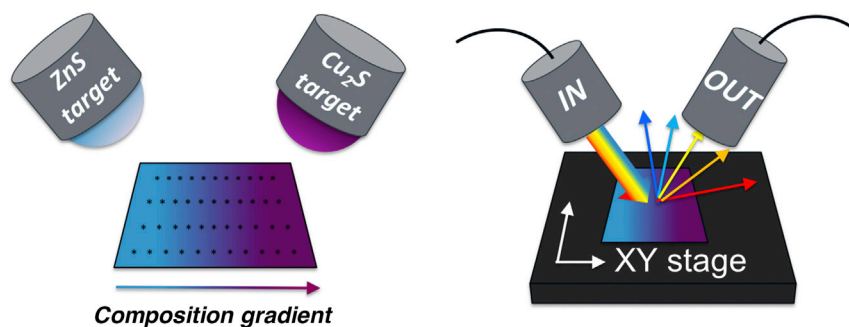


Figure 1. Combinatorial Synthesis and Characterization Schematic

Left: a schematic of the combinatorial sputter synthesis setup, consisting of a ZnS and a Cu_2S target at two individual sputter guns and a 50×50 mm sample “library” containing a composition gradient across the x axis. Right: a generalized schematic of the point-by-point characterization methodology, applied to study composition, crystalline phase, and optoelectronic properties.

between insulating, semiconducting, and metallic properties. Thus, we refer to this ternary space simply as “ $\text{Cu}_x\text{Zn}_{1-x}\text{S}$ ” herein, as is common in the literature, yet we acknowledge sulfur concentration $1 - \delta$ is also relevant. Using customized high-throughput combinatorial characterization tools, e.g., synchrotron diffraction, UV-visible near-infrared (UV-vis-NIR) spectrophotometry, and four-point probe resistivity measurements, as depicted in Figure 1B, we demonstrate that heterovalent, heterostructural alloying occurs within this compound, and observe the stabilization of the metastable WZ ZnS phase in the approximate region $0.19 < x < 0.50$. The transition from the ZB to WZ phase around $x = 0.19$ is found to correlate with increased conductivity and a decrease in absorption coefficient, and understanding these structure-property relations provides guidelines on how to improve transparency and conductivity in future work. We contextualize our findings across the literature space of $\text{Cu}_x\text{Zn}_{1-x}\text{S}$, comparing the reported phases, synthesis methods, and achieved properties.

RESULTS

Structure and Composition

Sample stoichiometry of >350 data points in eight combinatorial libraries spans almost all of the cation composition space of $\text{Cu}_x\text{Zn}_{1-x}\text{S}$, with $0 \leq x \leq 1$ where $x = \text{Cu}/(\text{Cu} + \text{Zn})$. Sulfur concentration ($1 - \delta$ in $\text{Cu}_x\text{Zn}_{1-x}\text{S}_{1-\delta}$) versus copper concentration x is plotted in Figure 2A (see Supplemental Information for calibration). Some regions have overlapping libraries and others have no data. Endpoint films with $x = 0$ are S-poor with respect to ZnS, with $1 - \delta = 0.92 \pm 0.04$ rather than $1 - \delta = 1$. Endpoint $x = 1$ aligns with a stoichiometry somewhere between $\text{Cu}_{1.2}\text{S}$ and $\text{Cu}_{1.4}\text{S}$, which is S-rich with respect to the nominal Cu_2S of the target. In all alloy films with $x > 0$ and $x < 1$, $1 - \delta$ appears to align approximately with that expected from an alloy of $\text{ZnS}:\text{Cu}_{1.6}\text{S}$, within measurement uncertainty. These findings corroborate literature findings of S-poor ZnS³⁷ and S-rich Cu_2S ,^{38,39} although S content is rarely reported. We observe a minor library-dependent effect such that data points from different sample libraries with the same x have slightly offset $1 - \delta$. These off-stoichiometries may stem from unintentional substrate heating from the plasma, from other non-equilibrium effects, or from a mixed oxidation state of Cu. Although energy-dispersive X-ray spectroscopy (EDS) measurements suggest oxygen contamination of less than 2%, this is presumed to only reside on the surface as a thin oxidized layer, which is expected because of air exposure of films. Bulk oxygen is undetectable via Rutherford backscattering spectrometry (RBS).

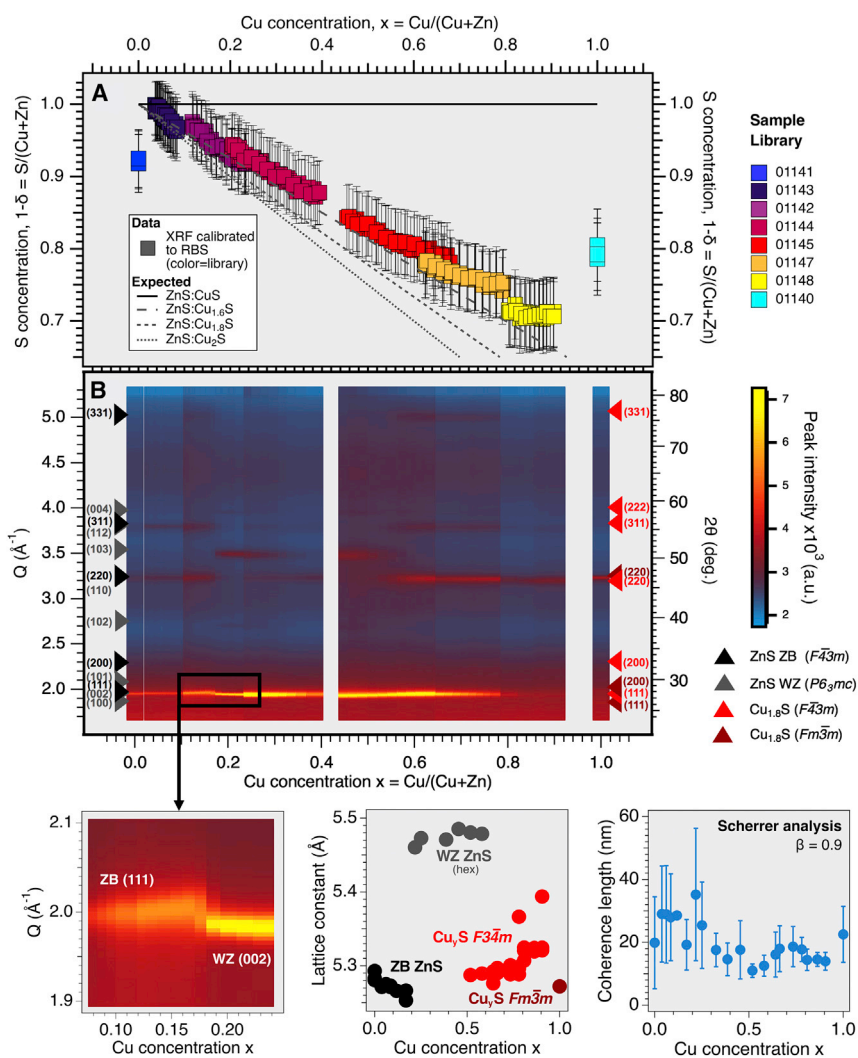


Figure 2. Chemical Composition and Crystal Structure Across $\text{Cu}_x\text{Zn}_{1-x}\text{S}$ Phase Space

(A) Calibrated S concentration $1 - \delta$ as a function of Cu concentration x for each combinatorial $\text{Cu}_x\text{Zn}_{1-x}\text{S}$ sample "library." Error bars are derived from uncertainty in RBS fitting procedure (see Supplemental Information).

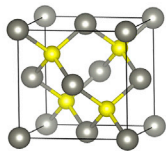
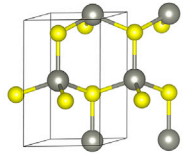
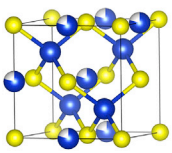
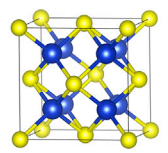
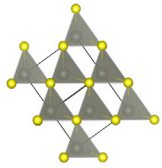
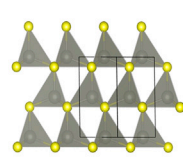
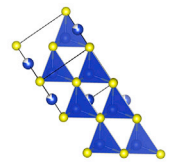
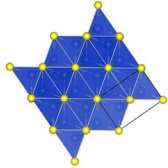
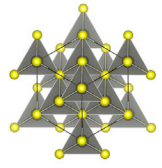
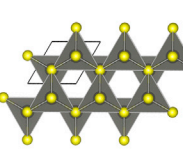
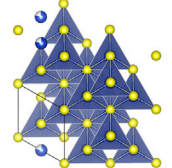
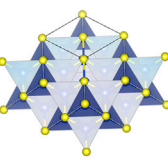
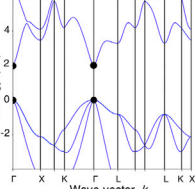
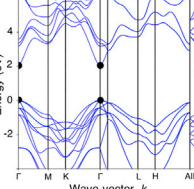
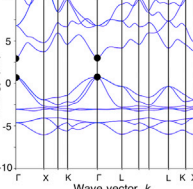
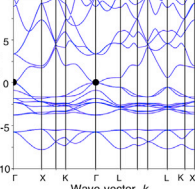
(B) Synchrotron X-ray diffraction measurements of ambient-temperature-synthesized $\text{Cu}_x\text{Zn}_{1-x}\text{S}$ films from $0 \leq x \leq 1$. Triangles indicate the dominant peaks of the four different crystal phases that are visible across the ternary phase space.

(C) Close-up of the zinc blende (ZB) (111) and wurtzite (WZ) (002) peaks in the region $1.9 \text{ \AA}^{-1} < Q < 2.1 \text{ \AA}^{-1}$, distinguishing the separate reflections. These are the directions of high orientation.

(D) Estimate of lattice constant from diffraction peak position. The label "hex" is to distinguish that the lattice constant for WZ structure stems from its hexagonal unit cell, and thus is larger than the others.

(E) Estimate of coherence length from Scherrer analysis, using the full width at half maximum of the dominant diffraction peaks and error bars estimated from the uncertainty in peak fit (see Supplemental Information).

In Figure 2B, we plot the synchrotron X-ray diffraction intensities (color scale) of the ambient-temperature-synthesized films as a function of cation composition x , with both Q and 2θ on the y axis (calibrated to Cu K- α emission wavelength) for reference. The amorphous halo around $Q = 2 \text{ \AA}^{-1}$ is due to the glass substrate. Broad peaks indicate a nanocrystalline film.

| | ▲ | ▲ | ▲ | ▲ |
|--|---|---|--|---|
| Structure | ZB ZnS | WZ ZnS | Cu_yS | Cu_yS |
| <i>Space group</i> | $F\bar{4}3m$ | $P6_3mc$ | $F\bar{4}3m$ | $Fm\bar{3}m$ |
| <i>Materials Project ID</i> | mp-10695 | mp-560588 | mp-760381 ($y = 1$) | mp-12087 ($y = 2$) |
| Cu concentration $x = \text{Cu}/(\text{Cu}+\text{Zn})$ | $0.0 \leq x \leq 0.19$ minor: $0.30 \leq x \leq 0.40$ | $0.19 \leq x \leq 0.50$ minor: $0.50 \leq x \leq 0.60$ | $0.60 \leq x \leq 0.90$ minor: $0.50 \leq x \leq 0.60$ | $x \approx 1.0$ |
| Cation local environment | Corner sharing tetrahedra (4) | Corner sharing tetrahedra (4) | Corner sharing tetrahedra (4) and octahedra (6) | Face sharing tetrahedra (4) |
| S local environment | Corner sharing tetrahedra (4) | Corner sharing tetrahedra (4) | Varies depending on y (4-8) | Square prismatic (8) |
| Unit cell |  |  |  |  |
| Polyhedra edge view |  |  |  |  |
| Polyhedra corner-centered view |  |  |  |  |
| GGA band structure |  |  |  |  |
| Average hole effective mass* | 0.794 | 1.255 | 0.004 | 0.591 |

* computed BoltzTraP effective mass at 300 K and $\rho = 10^{20} \text{ cm}^{-3}$

Figure 3. Schematic of the Four Crystal Structures Found in the Phase Space of $\text{Cu}_x\text{Zn}_{1-x}\text{S}$

"Cu concentration" denotes the composition for which each crystal structure appears. Colored triangles correspond to the phases in Figure 2. Space group information is given, local environment coordination is summarized, and structures are depicted in unit cell, polyhedra edge view, and polyhedra corner-centered view configurations to aid visualization of structural units. Computed GGA band structure from the Materials Project database⁴⁰ and average BoltzTraP-derived hole effective masses are also reported.^{41,42}

Within the phase space of $\text{Cu}_x\text{Zn}_{1-x}\text{S}$ we observe four distinct binary crystal structures: cubic zinc blende ZnS-type (space group $F\bar{4}3m$, denoted “ZB”), hexagonal wurtzite ZnS-type (space group $P6_3mc$, denoted “WZ”), Cu_yS -type ($1.6 \leq y \leq 2$; space group $F\bar{4}3m$), and Cu_yS -type ($1.2 \leq y \leq 1.4$; space group $Fm\bar{3}m$). These crystal structures, the Cu concentrations in which they are present, local coordination environments, theoretical GGA band structures (from the Materials Project database),⁴⁰ and BoltzTraP effective masses from a computational database^{41,42} are illustrated in Figure 3. The dominating diffraction peaks of these phases are marked in Figure 2B using colored triangles. Interestingly, the ratio of binary constituents does not change monotonically across x , in contrast to other low-temperature syntheses of $\text{Cu}_x\text{Zn}_{1-x}\text{S}$, e.g., CBD.²² There is also no evidence of a unique ordered ternary phase of all three elements, corroborated by the lack of such a thermodynamically stable phase in the Inorganic Crystal Structure Database or Materials Project database (although an ordered $F\bar{4}3m$ alloy may be possible around $x = 0.6$; cf. Supplemental Information for computational structure prediction).⁴⁰ Rather, this system appears to be a heterovalent, heterostructural alloy, with distinct regions in composition space where the structure transitions either sharply or gradually to another phase. One particular difficulty in identifying these phases arises from the similar symmetry, coordination, atomic radius, and unit cell size of ZB ZnS and cubic Cu_yS . Coupled with broad peaks, this results in nearly identical X-ray reflection locations, albeit slightly distinct relative intensities. For example, ZnS is less atomically dense in the (111) plane in comparison, so the peak at $Q = 2.0 \text{ \AA}^{-1}$ is fainter; we will be focusing on this peak subsequently.

At $x = 0$ (far left of Figure 2B) and from $0 \leq x \leq 0.18$, diffraction peaks correspond to ZB ZnS, with a faint shoulder peak at approximately $2\theta = 27^\circ$ suggestive of WZ ZnS (100). Films are nanocrystalline, yet somewhat oriented in the (111) direction. Between $0.10 < x < 0.19$, the (111) peak shifts slightly to higher 2θ by approximately 0.2° , as observed in Figure 2C. This correlates to the contraction of lattice parameter plotted in Figure 2D, which is expected upon Cu incorporation into ZnS, although the peak shift is lower in magnitude than the expected theoretical contraction of complete substitution of Cu_{Zn} antisites.²⁰ However, at approximately $x = 0.19$, the cubic peaks and the shoulder disappear and sharply transition to peaks indicative of (002) oriented WZ ZnS, as shown most discernibly by the appearance of the (103) WZ peak at approximately $Q = 3.5 \text{ \AA}^{-1}$ (approximately $2\theta = 51^\circ$). The large peak around $Q = 2.0 \text{ \AA}^{-1}$ ($2\theta = 28.5^\circ$) remains dominant, although it shifts noticeably to slightly lower values (see Figure 2C). It aligns with both WZ (002) and ZB (111), but is too broad to resolve. The intensity of the peak suggests (002) orientation, although could also discern some ZB still in the material. The WZ phase is present until $x = 0.50$, although a cubic $F\bar{4}3m$ phase appears briefly in the middle of this regime from approximately $0.30 < x < 0.40$, and could be from ZB ZnS or some ordered ternary $F\bar{4}3m$ structure, e.g., $F\bar{4}3m \text{ Cu}_2\text{ZnS}_2$ (see Supplemental Information).

Between $x = 0.50$ and $x = 0.60$, a gradual shift from WZ to cubic $F\bar{4}3m$ occurs in what appears to be a phase-separated composite of WZ ZnS and cubic Cu_yS . The peak around $Q = 2.0 \text{ \AA}^{-1}$ shifts to higher Q . We note the similarity with the ZB ZnS phase, and it is plausible there is mixed ZB ZnS within this regime. The diffraction patterns remain relatively unchanged from $0.60 < x < 0.90$, although the cubic (111) peak becomes fainter while the cubic (220) peak gets stronger with x . This could correspond to a shift in orientation. We deduce a phase change from $F\bar{4}3m \text{ Cu}_y\text{S}$ to what is likely an $Fm\bar{3}m$ structure somewhere between $x = 0.90$ and $x = 1$, but the onset is unclear. This phase is highly oriented in the (220) direction and is measured with RBS as Cu_yS with $1.2 \leq y \leq 1.4$. This is more S-rich than the Cu_2S target. We see no evidence of

covellite or chalcocite, the thermodynamic ground-state Cu_yS structures, nor any unique ternary phase across the entire phase space. In [Supplemental Information](#) we show patterns from higher-temperature synthesis conditions. In contrast to ambient-temperature-synthesized films, sputtered films at temperatures 180°C and greater clearly phase segregate into ZB ZnS and cubic $Fm\bar{3}m$ Cu_yS with larger grain sizes.

Coherence length of sample grains is estimated from the wide-angle X-ray scattering (WAXS) patterns using Scherrer analysis in [Figure 2E](#).⁴³ Across the full phase space, coherence length ranges from approximately 10 nm to 50 nm, with a slight decrease as x increases. Error bars stem from uncertainty in peak fit. It is highest within the WZ dominated films, suggesting larger grains. Due to peak broadening, Scherrer analysis is useful to estimate a lower limit to grain size.

Transmission electron microscopy (TEM) was performed for samples with approximately $x = 0.18$ and $x = 0.21$, selected as representative compositions that lie before and after the ZB-to-WZ phase transition, respectively, and within the TC regime. [Figures 4A](#) and [4B](#) show TEM bright-field images, [Figures 4C](#) and [4D](#) selected area electron diffraction (SAED) patterns, and [Figure 4E](#) integrated SAED patterns compared with the WAXS diffraction patterns. We find SAED patterns to corroborate our WAXS measurements, confirming the dominance of the ZB structure at $x = 0.18$ and WZ structure at $x = 0.21$. Furthermore, a Rietveld refinement analysis suggests that both samples contain approximately 5%–10% of secondary phases of WZ and ZB, respectively. This could explain the shoulder peak in ZB films. Additionally, both films appear to be polycrystalline. Comparison of [Figures 4C](#) and [4D](#) illustrates that the ZB phase contains relatively randomly oriented grains, as indicated by its diffraction rings, but in contrast the oriented diffraction spots in the WZ phase indicate high texturing in the (002) direction, corroborating the diffraction patterns. This is not unusual for WZ thin films in general, but somewhat surprising for thin films synthesized at ambient temperature, especially on glass substrates.

TEM micrographs show grain sizes on the order of 20 nm in width for the $x = 0.18$ and $x = 0.21$ samples, comparable with WAXS Scherrer analysis. TEM also illustrates the samples' growth in columnar grains (see [Supplemental Information](#)), which is typical for sputtered films.⁴⁴ We also note that EDS line scans and mapping do not detect any evidence of a phase-segregated Cu_yS at either of the two compositions studied (see [Supplemental Information](#)). There are some regions in each sample of compositional heterogeneity, mostly congregated at the surface, although this is most likely due to spurious particles released from the degrading copper sulfide sputtering target during growth.⁴⁵

Optical Properties

The optical absorption coefficient (α) is calibrated using film thickness and plotted for all Cu concentrations in [Figure 5A](#). Here, the y axis corresponds to incident photon energy and the color bar to α such that light colors indicate higher transparency. Note that the visible spectrum, approximately 390–750 nm, is equivalent to 1.65–3.17 eV and is notated with a rainbow bar. The purple color indicates the onset of the absorption edge, i.e., absorption coefficients of approximately 10^4 cm^{-3} , and the extent of the color gradient represents the sharpness of the edge. After a monotonic decrease with x of absorption onset from 3.4 eV to 3.1 eV, we observe a jump in absorption at approximately $x = 0.18$ up to 3.3 eV. A sharp drop in absorption onset occurs between Cu concentrations of 0.18 and approximately 0.35, followed by a more gradual monotonic decrease until $x = 1$ (with a slight jump likely due to a

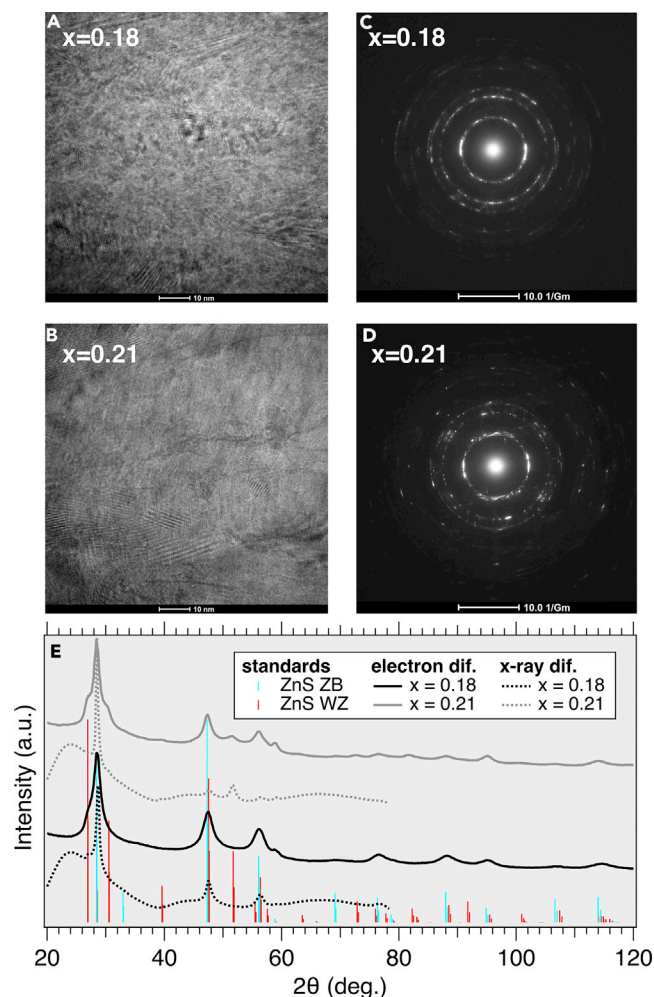


Figure 4. Transmission Electron Microscopy (TEM) Measurements of $\text{Cu}_x\text{Zn}_{1-x}\text{S}$

(A–D) TEM bright-field images for two distinct cation concentrations of $\text{Cu}_x\text{Zn}_{1-x}\text{S}$, with 10 nm scale bars: (A) $x = 0.18$ and (B) $x = 0.21$. Selected area electron diffraction patterns of (C) $x = 0.18$ and (D) $x = 0.21$, with 10.0 1/Gm scale bars. See [Supplemental Information](#) for labeling of rings corresponding to ZnS zinc blende (ZB) and wurtzite (WZ).

(E) Azimuthally integrated electron diffraction profiles, contrasted with X-ray diffraction profiles from respective samples. Peaks from ZnS ZB and WZ standards are marked in blue and red, respectively.

restrengthening of the WZ ZnS phase). We note that films synthesized at higher temperatures experience a slight decrease in absorption onset (by approximately 0.15 eV) within the range $0.2 < x < 0.4$ (see [Supplemental Information](#)), likely due to presence of copper sulfide secondary phases.

In Tauc analysis of semiconductors, the band gap usually is defined as the absorption onset of band-to-band transitions, which tends to become dominant at absorption coefficients of approximately 10^4 cm^{-1} .⁴⁶ Accordingly, in [Figure 5B](#) we estimate the band gap of these films with a Tauc plot, in which each curve is fitted to a line from absorption coefficient values of 10^4 to 10^5 cm^{-3} , and the intersection of this line with the energy axis is taken to be the optical gap. Cation composition is shown on the color bar. These absorption edges correlate with the purple region in [Figure 5A](#), as expected. Thus, these compounds span the range of band gap between

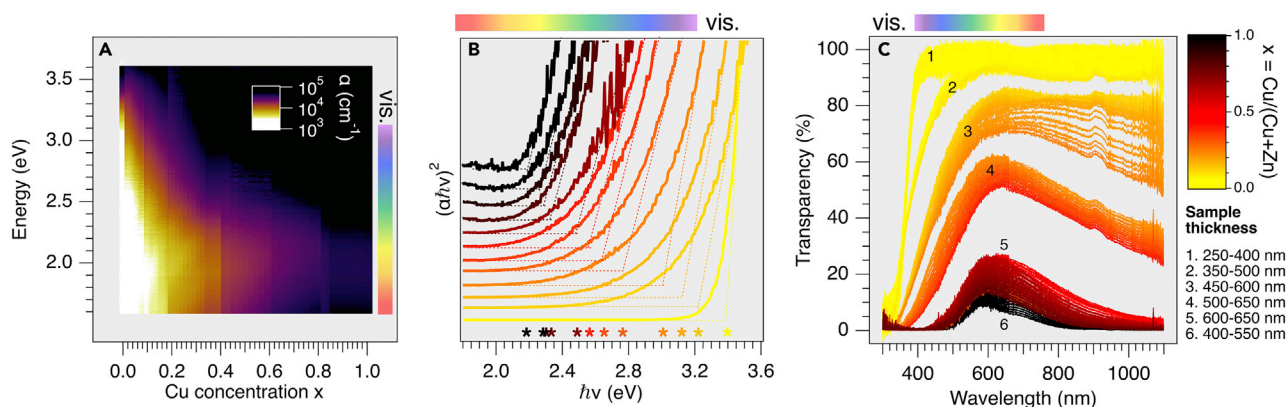


Figure 5. Optical Properties of $\text{Cu}_x\text{Zn}_{1-x}\text{S}$ Thin Films

(A) Optical absorption coefficient of $\text{Cu}_x\text{Zn}_{1-x}\text{S}$ samples, plotted as a function of incident photon energy and Cu concentration x .

(B) Tauc plots to estimate band gap in a representative set of cation compositions.

(C) Reflection corrected optical transparencies of six representative sample libraries across cation composition space. The rainbow bar indicates the visible spectrum.

approximately 3.4 eV for $x = 0$ through 2.2 eV for $x = 1$. This is as expected for insulating ZB ZnS and semimetallic Cu_yS . We observe Urbach tails in nearly all samples except $x = 0$ and $x = 1$.⁴⁷ This is not surprising, as we found small coherence lengths via Scherrer analysis and TEM, although it highlights a detrimental effect of small grains on optical transparency.

Figure 5C plots the reflection corrected optical transmittance in the UV-vis spectrum, also with cation composition plotted as the color bar (see Supplemental Information for derivation). $\text{Cu}_x\text{Zn}_{1-x}\text{S}$ films become significantly absorbent around $x = 0.4$. At $x > 0.4$, transmittance peaks around 600–650 nm and then decreases, likely due to an increase in plasma absorption and decrease in plasma wavelength in the NIR.⁴⁸ Quantitative comparison of these plots should be performed with caution, since thickness varies from 250 to 650 nm between samples and within individual samples due to thickness gradients of the combinatorial setup. This is rather thick for TC applications; functional n-type TCs for PVs, for example, typically vary from 20 to 200 nm,¹ so it is reasonable to assume higher transparencies are achievable for device applications.

Electrical Properties

In Figure 6C, we plot the electrical conductivity (σ) of >350 data points as a function of Cu concentration as measured by a combinatorial four-point probe (4pp) setup. Within the range $0 \leq x \leq 1$, hole conductivity ranges over at least five orders of magnitude, from less than $10^{-2} \text{ S cm}^{-1}$ at $x = 0.07$ to greater than $3 \times 10^3 \text{ S cm}^{-1}$ at $x = 1$. Conductivities of films $x < 0.07$ are below the detection limit of our instrument, since Hall measurements yield conductivities on the order of $10^{-2} \text{ S cm}^{-1}$ for $x = 0.05$ and $x = 0.07$ although error bars are as large as the measured value. Over the range $0 \leq x \leq 1$, conductivity essentially increases monotonically and can be subdivided into insulating, semiconducting (“TC regime”), and semimetallic regimes. However, sharp discontinuities in conductivity appear within the TC range at around $x = 0.19$ and $x = 0.40$ (although there is a gap in data for the latter). Conductivity spans from approximately 1 S cm^{-1} to 22 S cm^{-1} between $0.19 < x < 0.40$, respectively, jumps to around 150 S cm^{-1} at 0.45, and is greater than $1,200 \text{ S cm}^{-1}$ at $x = 0.80$. We note that within the TC regime, these are far from the highest conductivities achieved in the literature (see Perspective). Increasing the synthesis

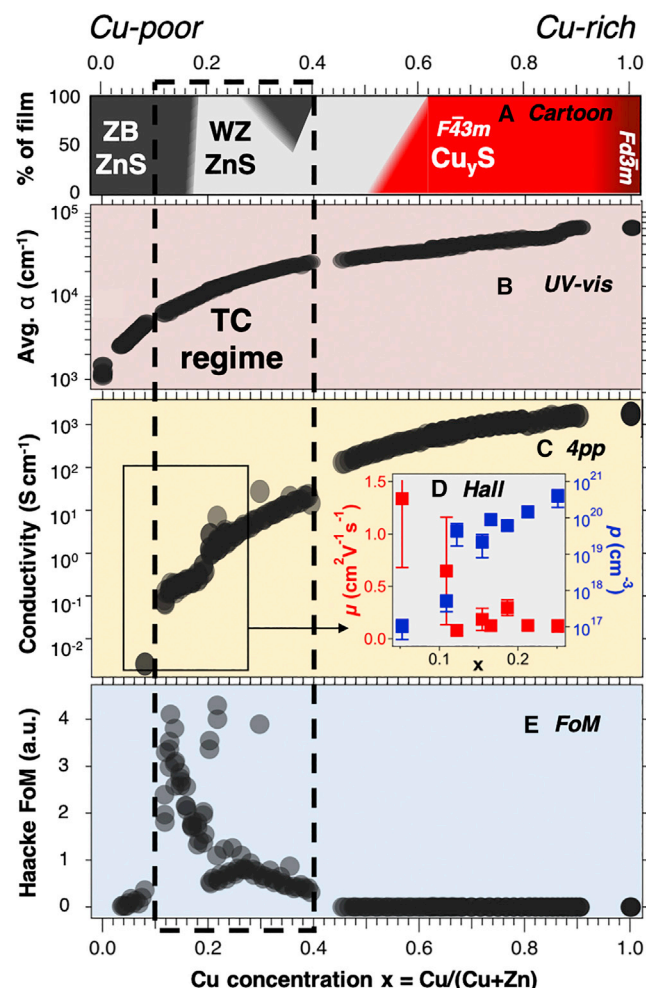


Figure 6. Comparison of Experimental Properties across the Phase Space of $\text{Cu}_x\text{Zn}_{1-x}\text{S}$, with $0 \leq x \leq 1$

- (A) Cartoon schematic of the various crystal phases: zinc blende (ZB) ZnS, wurtzite (WZ) ZnS, and two phases of cubic Cu_yS with $1.6 \leq y \leq 2$.
 (B) Optical absorption coefficient averaged over the visible spectrum (390–750 nm), as measured by UV-vis spectrophotometry (see Figure 5).
 (C) Hole conductivity measured by a four-point probe (4pp), depicting insulating, semiconducting, and metallic regimes.
 (D) Hole mobility and carrier concentration measured by a room-temperature Hall effect system with van der Pauw contacts, with statistical error bars from multiple measurements.
 (E) Haacke figure of merit (FoM), indicating the most optimal combination of properties in the “TC regime” ($0.1 \leq x \leq 0.4$) denoted with black dotted lines across the entire plot.

temperature to approximately 180°C yields a maximum conductivity of approximately 60 S cm^{-1} to 250 S cm^{-1} in the range $0.2 \leq x \leq 0.4$, respectively, which is approximately ten times higher than in samples synthesized at ambient temperature. However, this is a phase-separated material, and the high conductivity is most likely just due to the metallic Cu_yS phase.

The inset Figure 6D plots the Hall-derived hole mobility and hole concentration for a select set of compositions in the range $0.05 < x < 0.27$. All films are measured p-type. Hole concentration is shown to change over three orders of magnitude within this range, from $1.0 \pm 0.6 \times 10^{17} \text{ cm}^{-3}$ at $x = 0.05$ to $4 \pm 2 \times 10^{20} \text{ cm}^{-3}$ at $x = 0.27$,

increasing monotonically within the error bars of this measurement. This is not surprising, since conduction becomes more metallic as x increases and more carriers are introduced into the lattice. Meanwhile, mobility decreases with x but at a significantly slower rate, from approximately $1.3 \pm 0.7 \text{ cm}^2 \text{ V}^{-1} \text{ s}^{-1}$ at $x = 0.05$ to $0.12 \pm 0.06 \text{ cm}^2 \text{ V}^{-1} \text{ s}^{-1}$ at $x = 0.27$. Though generally decreasing, we observe a statistically significant jump in mobility somewhere in the approximate range $0.16 < x < 0.19$. We note that in semiconductors measured via conventional table-top DC Hall systems (room temperature, $< 2 \text{ T}$ magnetic field), mobilities below $1 \text{ cm}^2 \text{ V}^{-1} \text{ s}^{-1}$ have been shown to exhibit limited accuracy (our system uses a 0.3 T magnetic field), although systematic trends should be precise.⁴⁹ Additionally, the nature of combinatorial deposition adds another source of uncertainty to Hall measurements: since composition is not uniform over the probed area due to the combinatorial spread, measurements may convolute electrical properties from distinct compositions. For this reason, we cleave samples as small as possible ($5 \text{ mm} \times 5 \text{ mm}$) while retaining a uniform square shape with indium van der Pauw contacts.

Figure of Merit

Various formulas to calculate a figure of merit (FoM) for TCs have been proposed in the literature, although a standard FoM has not been agreed upon. Here, we select the FoM as proposed by Haacke, since it is one of the most widely used metrics:^{50,51}

$$\text{FoM} = T^q / R_{\text{sh}},$$

with q typically set to 10.³⁰ T is transmittance averaged over the visible regime (390–750 nm) and R_{sh} is sheet resistance in units of Ω/sq . We plot the Haacke FoM of our films in Figure 6E and find that the FoM function is maximized in an optimal transparent conducting regime, denoted “TC regime,” within approximately $0.10 < x < 0.40$. This corroborates the approximate range of optimized p-type transparent conducting properties found in the literature.²⁰ We note that the FoM is a useful metric for comparison, although it is not necessarily indicative of whether a TC will be useful for a particular application. We also note that the Haacke FoM is somewhat dependent on thickness, which is not constant across these samples.

DISCUSSION

Structural Phase Transitions and Influence on Optoelectronic Properties

We can now align the material properties of $\text{Cu}_x\text{Zn}_{1-x}\text{S}$ across cation chemical potential space in Figure 6 to highlight the distinct connection between structure, absorption, and hole transport. We will focus on the range $x \leq 0.4$. First, ZB ZnS is insulating at $x = 0$, with resistivities too small to measure. It is well established in the literature that, at even dilute concentrations of Cu, ZnS converts from n-type intrinsic behavior (due to interstitial Zn_i , or S vacancies, V_S) to p-type behavior (due to Cu_{Zn} antisite defects).^{15,52} Thus $\text{Cu}_x\text{Zn}_{1-x}\text{S}$ becomes semiconducting and p-type in low Cu concentrations of $0 < x < 0.10$. Carrier concentration is measured on the order of 10^{17} cm^{-3} in this range and increases with x by several orders of magnitude, indicative of activated carriers, while mobility drops by at least half. The slight lattice constant reduction in the approximate range $0.10 \leq x < 0.19$, see Figure 2C, provides evidence of Cu alloying into the ZB ZnS lattice, likely substituting for Zn on tetrahedral sites. Cu_{Zn} has been predicted to be a shallow acceptor,¹⁹ so as the site density increases, hole conductivity slowly increases. The introduction of Cu_{Zn} has been shown to raise the valence band, reduce the band gap, and contribute tail states to the band edges due to Cu 3d orbitals, so this increase in absorption is reasonable.⁵³ Previous studies have postulated that above its solubility limit Cu ions phase segregate to form amorphous or nanocrystalline Cu_yS , but we see no evidence of this in EDS line scans at $x = 0.18$ (see

Supplemental Information).²⁰ It is possible that excess S or Cu are occupying interstitial sites, or that defect complexes are forming to counteract lattice contraction. We can look toward the breadth of literature on $\text{Cu}_2\text{ZnSnS}_4$ (i.e. CZTS, essentially this compound with added Sn) to estimate the defect physics, in particular the high probability of disorder between the Cu and Zn to produce Cu_{Zn} and Zn_{Cu} .⁵⁴ Like CZTS, we observe Cu^{+1} cations in our structures and claim that Cu_{Zn} leads to p-type conductivity. However, we caution directly transferring CZTS defect physics due to the influence of Sn, and recommend in-depth defect calculations to confirm specific behavior.

The jump to higher conductivity at approximately $x = 0.19$, which is systematically reproduced across multiple libraries, correlates with the shift to the WZ ZnS crystal structure at the same stoichiometry. Mobility appears to increase moderately at this Cu concentration as well. We also observe a reduction in short wavelength absorption, demonstrated by the purple spike in Figure 5A, although the average absorption coefficient remains relatively smooth as evident in Figure 6B. This is reasonable because the band gap of WZ ZnS has been demonstrated to be approximately 0.1–0.4 eV greater than that of ZB ZnS. A second jump in conductivity between 0.40 and 0.45 correlates to a restrengthening of the signal of the WZ (103) reflection. We expect that the Cu atoms have substituted for Zn at tetrahedral sites in this regime as well. This corroborates the presence of a WZ onset and elevated conductivity in PLD synthesized films, although the shift to the WZ phase occurs at a slightly higher Cu content of $0.25 < x < 0.30$.²⁰ It also seems reasonable Cu could occupy octahedral voids, as it does in $\text{Cu}_{1.8}\text{S}$. The observed increases in both conductivity and absorption after $x = 0.5$, as Cu_yS phases start to dominate, is expected as the film becomes more metallic.

The results presented in this article lead to two interesting questions. (1) Why do we observe a heterostructural alloy system with the onset of a WZ phase, rather than a cubic isostructural alloy or nanocomposite? (2) Why does the presence of the WZ phase seem to correlate to higher hole transport? First, we discuss why the WZ phase may be structurally favorable. The most likely argument we find is a strain-induced phase transformation. Previous studies of alloys have exploited induced surface strain to catalyze growth of metastable "negative pressure" polymorphs.⁵⁵ For example, in the ZnS-ZnTe and AlP-AlSb systems it has been observed that alloying two ZB structures can stabilize a WZ structure (e.g., $\text{ZnS}_x\text{Te}_{1-x}$) due to lower strain energies and formation enthalpies.⁵⁶ Moreover, our group has recently stabilized metastable WZ phases in $\text{Mn}_{1-x}\text{Zn}_x\text{Te}$ alloys.⁵⁷ WZ polymorphs of compounds with ZB or rocksalt stable phases have been routinely observed in nanowires, and the consensus is that the interfacial energy and strain is responsible in these cases as well.⁵⁸ It also is surprising that WZ ZnS is present in ambient-temperature-synthesized films, since the ZB-to-WZ phase transition occurs in single crystals at atmospheric pressure between 800°C and 1,020°C.^{59,60} However, it has been shown that the formation energy of this transition can be reduced significantly in nanoparticles and thin films due to surface strain.⁶¹

Additionally, it is possible that Cu is more soluble in the WZ than the ZB phase, such that a structural transition is induced at a critical Cu content where ZB can no longer support the quantity of Cu. Another related possibility that merits consideration is the approach of a percolation threshold within ZnS, i.e., a connected network of Cu throughout the crystal. This percolation threshold is expected at approximately $x = 0.20$, assuming random occupancy of Cu on the Zn sites and an fcc lattice.⁶² It is possible that the WZ phase becomes stabilized at this percolation discontinuity,

although more in-depth analysis is required to explain the exact cause of the structural shift. Furthermore, sputtering is a non-equilibrium synthesis method, so in addition to induced alloy strain the presence of high-energy ion fluxes at the substrate surface can induce formation of metastable, high-temperature phases.⁶³ We postulate that low-temperature films are able to access a local minimum of formation energy just above a miscibility gap where the formation of a heterostructural alloy is more preferable than spinodal decomposition into multiple phases.⁶⁴ To assist the understanding of WZ stabilization within the Cu-Zn-S system, formation energy calculations must be performed, but are beyond the scope of this investigation.

Second, we discuss how the presence of the WZ ZnS phase is correlated with higher hole transport. The reason for this is not entirely clear. In fact, this finding is counter-intuitive in that the average hole effective mass of WZ ZnS is 1.25 while that of ZB ZnS is approximately 0.79 (see [Figure 3](#), as estimated by the BoltzTraP code for hole dopings of 10^{20} cm^{-3} at 300 K).⁴² This would suggest larger achievable hole mobilities in ZB, yet we observe the opposite in experiments. It is possible that the solubility of Cu in WZ is higher than in ZB, or donor “hole killer” compensation is lower, leading to higher carrier concentrations. However, we propose it is most likely that microstructural mechanisms explain our findings. We observe larger grains and higher texturing in the WZ phase, which could reduce grain boundary scattering and increase hole mobility. TEM shows no presence of a Cu_yS matrix within the $x = 0.21$ film, which has been a proposed mechanism of elevated conductivity for past studies of $\text{Cu}_x\text{Zn}_{1-x}\text{S}$,^{20,22} although we cannot rule out this possibility of a secondary phase within the region $0.40 < x < 0.45$. We also acknowledge defect density, S off-stoichiometry, tolerance to cation disorder, or oxygen incorporation as possible sources of the jump in hole conductivity, although this is less likely because the local coordination environments are similar in ZB and WZ ZnS phases (see [Figure 3](#)). However, more in-depth measurements of hole mobility and defect concentration are necessary to quantify this effect.

Perspective

To contextualize our findings and highlight previous studies on this material, we compared properties of $\text{Cu}_x\text{Zn}_{1-x}\text{S}$ reported in the literature in [Figure 7](#).^{19–24,28,37,65–69} Marker shapes denote the phase reported in each study, which are all alloys except for the ZnS + CuS composite system (triangles), while the color indicates the reported Cu concentration. Samples from the literature are denoted with thin outlines, while those from this study have thick outlines. The literature samples span a wide range of chemical potential space; we only plot those with reported band gaps here, but include a table with data and references of both these studies and those without complete properties in [Supplemental Information](#).^{25–27,29,70–78} For comparison, we also plot typical values of band gap and conductivity for n-type Sn-doped In_2O_3 (ITO)⁷⁹ and one of the highest performing p-type TCs, Mg-doped CuCrO_2 .⁸⁰

Our films are lower in conductivity than the highest reported in the literature (note that the triangular samples are from elevated synthesis temperatures with phase segregation). One reason for this may be the sulfur deficiency in the TC regime with respect to an expected ZnS:CuS alloy, leading to substantial carrier compensation from sulfur vacancies. We note that anion concentration ($\delta - 1$ in $\text{Cu}_x\text{Zn}_{1-x}\text{S}_{\delta-1}$) and oxygen impurities are not plotted here, nor are they reported in all but one study. Film thickness is also not plotted, which can significantly influence optoelectronic properties. Our findings suggest guidelines for improved performance, which requires a simultaneous reduction of scattering, increase of hole doping, and

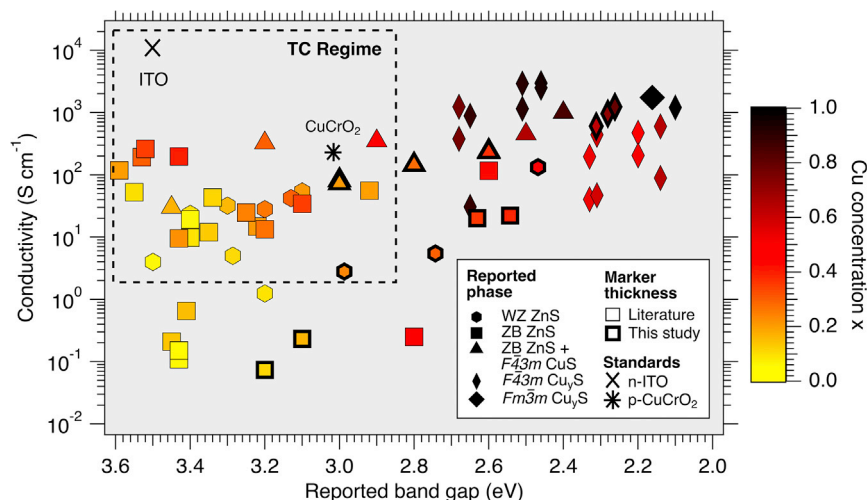


Figure 7. Electrical and Optical Properties of $\text{Cu}_x\text{Zn}_{1-x}\text{S}$ Reported in the Literature

Realized optoelectronic properties of the $\text{Cu}_x\text{Zn}_{1-x}\text{S}$ phase space across all literature studies, from 2009 to 2018, highlighting conductivity as a function of band gap (Cu concentration is the color bar).^{19–24,28,37,65–69} The marker shape depicts the reported crystalline phase. Thin lines indicate samples from the literature, while thick lines indicate a representative set of samples from this study. All reported phases are alloys or doped, except for the ZnS + CuS composite (phase-segregated) system.

maintenance of a high-absorption onset. First, a higher growth temperature or an anneal step is recommended to increase grain size, limit grain boundary scattering, and increase hole mobility. Annealing has been performed in the literature,^{23,66} but has been demonstrated only to increase conductivity by one report, to our knowledge.²¹ A downside of high growth temperature is a lack of compatibility in applications with low thermal budgets and possible ZnS and Cu_3S phase segregation. Second, V_S can compensate hole concentration, so filling vacancies should increase carrier concentration. This can be done by increasing anion chemical potential during growth by, e.g., cracking sulfur-containing gas or annealing in an S-rich environment. Third, in sputtering specifically, we recommend continuing to optimize growth pressure, gun position, and gas flow rate. As evidenced from the recent high conductivity and transparency,²¹ the Cu-Zn-S system has the potential for even greater performance upon process optimization.

Whether an alloy or composite forms in $\text{Cu}_x\text{Zn}_{1-x}\text{S}$ depends on thermodynamic growth conditions; we have shown that this depends also on anion concentration, as we primarily make alloys except in the region $0.5 < x < 0.6$. It is observed in Figure 7 that the physical deposition methods at low temperatures tend to result in an alloy, while chemical deposition tends to yield phase-separated materials at both high and low temperatures. Sputtering and PLD yield relatively similar film qualities and properties; specifically, both methods lean toward alloy formation. However, PLD is capable of perturbing synthesis even further from equilibrium due to its high incident laser energy. This may result in increased solubility of Cu and other non-equilibrium effects that could lead to higher conductivities. Direct comparison of these methods is beyond our scope, but we refer the interested reader to comprehensive references.^{13,81–83} Thus, the choice of synthesis method and temperature matter, and can be tuned to the application of interest. We also expect a distinction in band alignment of phase-separated systems in comparison with alloy systems, since electronic states from both phases will contribute to band edges. This may

present an issue in electronic devices, so alloyed phases may be advantageous for optoelectronic applications. This investigation motivates the need for follow-up work to calculate and measure band offsets using density functional theory and X-ray photoelectron spectroscopy, among other methods.

Conclusion

In this study, $\text{Cu}_x\text{Zn}_{1-x}\text{S}$ was synthesized at ambient temperature across the entire cation composition space $0 \leq x \leq 1$. We have created the first full-range map of diffraction patterns across this space, charting four distinct crystal structures. A relatively transparent semiconducting regime is achieved in the range $0.1 < x < 0.4$, consisting of ZB ($0.1 < x < 0.19$) and WZ ZnS ($0.19 < x < 0.4$) regimes with conductivities of approximately 3 S cm^{-1} for a band gap of 3 eV. This aligns with optimized transparent conducting regimes of previous studies. Conductivities over $1,000 \text{ S cm}^{-1}$ were achieved in a semimetallic regime at $x = 0.80$, consisting mostly of a cubic Cu_yS phase. We observe a jump in conductivity around $x = 0.19$, which correlates with the onset of a large-grain, highly textured WZ phase. This is surprising at such low temperatures and in the middle of a cubic alloy system. Our analysis suggests the importance of the WZ phase in achieving highly conductive alloys in the transparent region. Evidently it is the large, oriented grains of the WZ structure that are responsible for this elevated conductivity; this suggests, not surprisingly, that achieving larger grains should increase conductivity, although there is a trade-off with increasing synthesis temperature. Although alloying occurs in these low-temperature sputtered films, we find that growth at temperatures of 180°C and higher yields phase separation. The properties of the ambient-temperature films from this study are similar to those from other sputtering and PLD reports, but they are not likely representative of the phase space of other synthesis methods. To illustrate the differences, we have compared our results with those from the literature, suggesting different microstructure and conductivity mechanisms in $\text{Cu}_x\text{Zn}_{1-x}\text{S}$ thin films synthesized via various methods.

Investigation into the role of defects and disorder within this phase space, as well as investigation of band alignment and band bending within this system, could provide further insight into properties to optimize performance within the TC regime. Although this study has focused on the role of cation composition, we acknowledge that the interplay of anion off-stoichiometries and Cu nominal oxidation state is also key to elucidating structure-property relations of the entire ternary phase space of $\text{Cu}_x\text{Zn}_{1-x}\text{S}_{1-\delta}$. Additionally, we have synthesized primarily ambient-temperature films due to their remarkable properties and potential applications in low thermal budget systems, but an understanding of temperature stability and phase transformations is an important next step. There exist a variety of proposed p-type TCs in the literature, including oxide chemistries but also chalcogenides, e.g., $\text{Cu}_x\text{Zn}_{1-x}\text{S}$ and mixed oxychalcogenides, which have yet to be implemented into PV devices. $\text{Cu}_x\text{Zn}_{1-x}\text{S}$ demonstrates the materials design scheme of selecting two binary endpoints to tailor alloy properties toward new functionalities, and highlights that a unique metastable phases may lie between these two endpoints. Specifically, the generalized approach of combining one binary endpoint with high transparency and another with high hole conductivity, and exploring the resulting ternary phase space combinatorially, is a promising approach toward designing ternary p-type TC systems beyond $\text{Cu}_x\text{Zn}_{1-x}\text{S}$. Thus, this study highlights the importance of continuing in-depth, combinatorial studies in $\text{Cu}_x\text{Zn}_{1-x}\text{S}$ and beyond to map out the optimal performance space, correlate structure with optical and electrical properties, measure or calculate band alignment, and investigate stability. Such

understanding can then inform materials selection criteria and aid implementation into next-generation energy devices.

EXPERIMENTAL PROCEDURES

The combinatorial method⁸⁴ was used to sputter deposit eight thin-film combinatorial “libraries” of $\text{Cu}_x\text{Zn}_{1-x}\text{S}$ with gradients in cation composition, as depicted in Figure 1A. Precursor sputtering targets were 2-inch-diameter ZB ZnS and chalcocite Cu_2S . Films of thickness 250–600 nm were deposited via radiofrequency (RF) co-sputtering in an inert Ar environment, with vacuum base pressure 5×10^{-7} Torr, growth pressure 1.3×10^{-3} Torr, and RF power varying from 0 W to 40 W. Sample libraries were grown on 50×50 mm Eagle XG glass substrates with copper concentrations spanning the entire cation chemical potential space, i.e., Cu cation concentration $x = \text{Cu}/(\text{Cu} + \text{Zn})$ ranging from 0 to 1. Multiple libraries of the same composition gradient were synthesized to enhance statistical significance. Substrates were at ambient temperature during growth, i.e., with no active heating yet some unintentional heating due to plasma energy. As a comparison we also synthesized films at elevated temperatures of 185°C, 200°C, 250°C, and 330°C, within the limited composition range of approximately $0.2 < x < 0.4$ (see Supplemental Information).

Material properties were characterized with customized combinatorial measurement tools shown in Figure 1B. A 4×11 mapping grid resulted in 44 data points per library and >350 unique compositional data points in total. Film cation composition and thickness were determined using mapping-style X-ray fluorescence and Dektak profilometry. Structural analysis mapping was performed with WAXS on beamline 1-5 at the Stanford Synchrotron Radiation Lightsource (SSRL). 2D scattering was collected with a Rayonix 165 CCD Camera at grazing incidence at an incident energy of 12.7 keV, and peaks were integrated in the range $5^\circ < \chi < 175^\circ$. For Scherrer coherence length analysis, peaks were fit to a Voigt function. Electrical and optical properties were collected using a mapping-style custom-built four-point probe (4pp) and UV-vis-NIR spectrophotometry system with deuterium and tungsten/halogen light sources and Si and InGaAs detector arrays. Custom Igor Pro software was used to process and analyze combinatorial characterization data⁸⁵ and calculate derived properties such as conductivity and absorption coefficient. The source data supporting these analyses will be made publicly available through <https://htem.nrel.gov/>.⁸⁶

TEM micrographs were acquired for selected compositions with an FEI Talos F200X microscope with scanning capabilities operating at an accelerating voltage of 200 keV. Specimens for TEM were prepared from deposited films via *in situ* focused ion beam lift-out methods⁸⁷ using an FEI Helios Nanolab 600i SEM/FIB DualBeam workstation. Specimens were ion milled at 2 keV and 77 pA to remove ion beam damage, and thin films to approximately 80 nm. SAED patterns were collected on an FEI Ceta 16M pixel CMOS camera at a camera length of 410 mm for structural characterization. Platinum from the FIB was used to calibrate the camera constant, allowing SAED reflections to be accurately measured and indexed. Chemical composition was analyzed by TEM using a Super-X EDS system equipped with four windowless silicon drift detectors. RBS was performed on a National Electrostatics 3S-MR10 instrument with a 2 MeV alpha particle beam, and was used to determine anion concentration for select films using the SIMNRA analysis package.⁸⁸ A Bio-Rad HL5500 PC Hall effect instrument under a magnetic field of 0.3 T was used for selected samples, prepared with a van der Pauw contact configuration

on samples cleaved to 5 mm × 5 mm, to measure conductivity, mobility, and carrier concentration at room temperature.

DATA AND CODE AVAILABILITY

The accession numbers (unique identifiers) for the sample libraries reported in this paper are HTEM DB: 10073, 10089, 10072, 10071, 10070, 10091, 10088, 10093, 10087.

SUPPLEMENTAL INFORMATION

Supplemental Information can be found online at <https://doi.org/10.1016/j.matt.2019.06.019>.

ACKNOWLEDGMENTS

This work was supported by the US Department of Energy (DOE) under contract no. DEAC36-08GO28308 with Alliance for Sustainable Energy, the Manager and Operator of the National Renewable Energy Laboratory. Funding provided by Office of Science (SC), Office of Basic Energy Sciences (BES), as part of the Energy Frontier Research Center “Center for Next Generation of Materials Design: Incorporating Metastability.” R.W.-R. acknowledges PhD funding from the U.C. Berkeley Chancellor’s Fellowship and the National Science Foundation Graduate Research Fellowship Program under grant numbers DGE1106400 and DGE1752814. Y.H. is also supported by the Science and Technology Commission of Shanghai Municipality (no. 16JC1400603) and a grant from the National Natural Science Foundation of China (no. 61471126). Use of the SSRL, SLAC National Accelerator Laboratory, was supported by the DOE, SC, and BES under contract no. DE-AC02-76SF00515. The use of combinatorial thin-film synthesis and spatially resolved characterization facilities at NREL, as a part of High Throughput Experimental Materials Collaboratory (HTE-MC), is gratefully acknowledged. The authors thank Dr. Adele Tamboli, Dr. Angela Fioretti, Dr. John Perkins, Prof. Joel W. Ager III, Dr. Brenden Ortiz, and Dr. Matthew Horton for fruitful discussion.

AUTHOR CONTRIBUTIONS

Conceptualization, R.W.-R. and A.Z.; Methodology, R.W.-R. and A.Z.; Investigation, R.W.-R., Y.H., J.S.M., and C.L.M.; Writing – Original Draft, R.W.-R. and A.Z.; Writing – Review & Editing, all authors; Funding Acquisition, A.Z. and R.W.-R.; Resources, A.Z. and A.M.; Supervision, A.Z., K.A.P., and B.P.G.

DECLARATION OF INTERESTS

The authors declare no competing interests.

Received: February 22, 2019

Revised: May 22, 2019

Accepted: June 14, 2019

Published: September 4, 2019

REFERENCES

1. Delahoy, A.E., and Guo, S. (2011). *Handbook of Photovoltaic Science and Engineering*, Second Edition (Wiley Online Library), pp. 716–796.
2. Morales-Masis, M., De Wolf, S., Woods-Robinson, R., Ager, J.W., and Ballif, C. (2017). Transparent electrodes for efficient optoelectronics. *Adv. Electron. Mater.* 3, 1600529.
3. Hosono, H. (2007). Recent progress in transparent oxide semiconductors: materials and device application. *Thin Solid Films* 515, 6000–6014.
4. Huang, F.-Q., Liu, M.-L., and Yang, C. (2011). Highly enhanced p-type electrical conduction in wide band gap $\text{Cu}_{1+x}\text{Al}_{1-x}\text{S}_2$ polycrystals. *Sol. Energy Mater. Sol. Cells* 95, 2924–2927.
5. Liu, M.-L., Huang, F.-Q., Chen, L.-D., Wang, Y.-M., Wang, Y.-H., Li, G.-F., and Zhang, Q.

- (2007). p-type transparent conductor: Zn-doped CuAlS_2 . *Appl. Phys. Lett.* **90**, 072109.
6. Park, S., Keszler, D.A., Valencia, M.M., Hoffman, R.L., Bender, J.P., and Wager, J.F. (2002). Transparent p-type conducting BaCu_2S_2 films. *Appl. Phys. Lett.* **80**, 4393–4394.
 7. Han, Y., Siol, S., Zhang, Q., and Zakutayev, A. (2017). Optoelectronic properties of strontium and barium copper sulfides prepared by combinatorial sputtering. *Chem. Mater.* **29**, 8239–8248.
 8. Tate, J., Newhouse, P.F., Kykyneshi, R., Hersh, P.A., Kinney, J., McIntyre, D.H., and Keszler, D.A. (2008). Chalcogen-based transparent conductors. *Thin Solid Films* **516**, 5795–5799.
 9. Hiramatsu, H., Ueda, K., Ohta, H., Hirano, M., Kamiya, T., and Hosono, H. (2003). Degenerate p-type conductivity in wide-gap $\text{LaCuOS}_{1-x}\text{Se}_x$ ($x = 0-1$) epitaxial films. *Appl. Phys. Lett.* **82**, 1048–1050.
 10. Yanagi, H., Tate, J., Park, S., Park, C.-H., and Keszler, D.A. (2003). p-type conductivity in wide-band-gap BaCuQF ($Q = \text{S, Se}$). *Appl. Phys. Lett.* **82**, 2814–2816.
 11. Shi, J., Cerqueira, T.F., Cui, W., Nogueira, F., Botti, S., and Marques, M.A. (2017). High-throughput search of ternary chalcogenides for p-type transparent electrodes. *Sci. Rep.* **7**, 43179.
 12. Raghupathy, R.K.M., Kühne, T.D., Felser, C., and Mirhosseini, H. (2018). Rational design of transparent p-type conducting non-oxide materials from high-throughput calculations. *J. Mater. Chem. C* **6**, 541–549.
 13. Madelung, O. (2012). *Semiconductors: Data Handbook* (Springer Science & Business Media).
 14. Corrado, C., Cooper, J.K., Hawker, M., Hensel, J., Livingston, G., Gul, S., Vollbrecht, B., Bridges, F., and Zhang, J.Z. (2011). Synthesis and characterization of organically soluble Cu-doped ZnS nanocrystals with Br co-activator. *J. Phys. Chem. C* **115**, 14559–14570.
 15. Ummartyotin, S., Bunnak, N., Juntaro, J., Sain, M., and Manuspiya, H. (2012). Synthesis and luminescence properties of ZnS and metal (Mn, Cu)-doped-ZnS ceramic powder. *Solid State Sci.* **14**, 299–304.
 16. Ummartyotin, S., and Infahsaeng, Y. (2016). A comprehensive review on ZnS: From synthesis to an approach on solar cell. *Renew. Sustain. Energy Rev.* **55**, 17–24.
 17. Yang, K., and Ichimura, M. (2011). Fabrication of transparent p-Type $\text{Cu}_x\text{Zn}_y\text{S}$ thin films by the electrochemical deposition method. *Jpn. J. Appl. Phys.* **50**, 040202.
 18. Fang, X., Zhai, T., Gautam, U.K., Li, L., Wu, L., Bando, Y., and Golberg, D. (2011). ZnS nanostructures: from synthesis to applications. *Prog. Mater. Sci.* **56**, 175–287.
 19. Diamond, A.M., Corbellini, L., Balasubramaniam, K., Chen, S., Wang, S., Matthews, T.S., Wang, L.-W., Ramesh, R., and Ager, J.W. (2012). Copper-alloyed ZnS as ap-type transparent conducting material. *Phys. Status Solidi A* **209**, 2101–2107.
 20. Woods-Robinson, R., Cooper, J.K., Xu, X., Schelhas, L.T., Pool, V.L., Faghaninia, A., Lo, C.S., Toney, M.F., Sharp, I.D., and Ager, J.W. (2016). P-Type transparent Cu-alloyed ZnS deposited at room temperature. *Adv. Electron. Mater.* **2**, 1500396.
 21. Feng, M., Zhou, H., Guo, W., Zhang, D., Ye, L., Li, W., Ma, J., Wang, G., and Chen, S. (2018). Fabrication of P-type transparent conducting $\text{Cu}_x\text{Zn}_{1-x}\text{S}$ films on glass substrates with high conductivity and optical transparency. *J. Alloys Compd.* **750**, 750–756.
 22. Xu, X., Bullock, J., Schelhas, L.T., Stutz, E.Z., Fonseca, J.J., Hettick, M., Pool, V.L., Tai, K.F., Toney, M.F., Fang, X., and Ager, J. (2016). Chemical bath deposition of p-type transparent, highly conducting $(\text{CuS})_x(\text{ZnS})_{1-x}$ nanocomposite thin films and fabrication of Si heterojunction solar cells. *Nano Lett.* **16**, 1925–1932.
 23. Goktas, A., Aslan, F., and Tumbul, A. (2015). Nanostructured Cu-doped (ZnS) polycrystalline thin films produced by a wet chemical route: the influences of Cu doping and film thickness on the structural, optical and electrical properties. *J. Solgel Sci. Technol.* **75**, 45–53.
 24. Sreejith, M., Deepu, D., Kartha, C.S., and Vijayakumar, K. (2014). Tuning of properties of sprayed CuZnS films. *AIP Conf. Proc.* **1591**, 1741–1743.
 25. Jubimol, J., Sreejith, M., Kartha, C.S., Vijayakumar, K., and Louis, G. (2018). Analysis of spray pyrolysed copper zinc sulfide thin films using photoluminescence. *J. Lumin.* **203**, 436–440.
 26. Di Benedetto, F., Cinotti, S., D’Acapito, F., Vizza, F., Foresti, M.L., Guerri, A., Lavacchi, A., Montegrossi, G., Romanelli, M., Cioffi, N., and Innocenti, M. (2015). Electrodeposited semiconductors at room temperature: an X-ray absorption spectroscopy study of Cu-, Zn-, S-bearing thin films. *Electrochim. Acta* **179**, 495–503.
 27. Mahuli, N., Saha, D., Maurya, S.K., Sinha, S., Patra, N., Kavaipatti, B., and Sarkar, S.K. (2018). Atomic layer deposition of transparent and conducting p-Type $\text{Cu}(\text{I})$ incorporated [ZnS] thin films: unravelling the role of compositional heterogeneity on optical and carrier transport properties. *J. Phys. Chem. C* **122**, 16356–16367.
 28. Chamorro, W., Shyju, T., Boulet, P., Migot, S., Ghanbaja, J., Miska, P., Kuppasami, P., and Pierson, J. (2016). Role of Cu^+ on ZnS: Cu p-type semiconductor films grown by sputtering: influence of substitutional Cu in the structural, optical and electronic properties. *RSC Adv.* **6**, 43480–43488.
 29. Maurya, S.K., Liu, Y., Xu, X., Woods-Robinson, R., Das, C., Ager, J.W., and Balasubramaniam, K.R. (2017). High figure-of-merit p-type transparent conductor, Cu alloyed [ZnS] via radio frequency magnetron sputtering. *J. Phys. D Appl. Phys.* **50**, 505107.
 30. Ellmer, K. (2012). Past achievements and future challenges in the development of optically transparent electrodes. *Nat. Photonics* **6**, 809.
 31. Krebs, F.C., and Jørgensen, M. (2013). Polymer and organic solar cells viewed as thin film technologies: what it will take for them to become a success outside academia. *Sol. Energy Mater. Sol. Cells* **119**, 73–76.
 32. Subedi, K.K., Bastola, E., Subedi, I., Song, Z., Bhandari, K.P., Phillips, A.B., Podraza, N.J., Heben, M.J., and Ellingson, R.J. (2018). Nanocomposite $(\text{CuS})_x(\text{ZnS})_{1-x}$ thin film back contact for CdTe solar cells: Toward a bifacial device. *Sol. Energy Mater. Sol. Cells* **186**, 227–235.
 33. Li, J., Kuang, C., Zhao, M., Zhao, C., Liu, L., Lu, F., Wang, N., Huang, C., Duan, C., Jian, H., et al. (2018). Ternary CuZnS nanocrystals: synthesis, characterization, and interfacial application in perovskite solar cells. *Inorg. Chem.* **57**, 8375–8381.
 34. Xu, X., Chen, J., Cai, S., Long, Z., Zhang, Y., Su, L., He, S., Tang, C., Liu, P., Peng, H., et al. (2018). A real-time wearable UV-radiation monitor based on a high-performance p-CuZnS/n-TiO₂ photodetector. *Adv. Mater.* **30**, 1803165.
 35. Cai, J., Xu, X., Su, L., Yang, W., Chen, H., Zhang, Y., and Fang, X. (2018). Self-powered n-SnO₂/p-CuZnS core-shell microwire UV photodetector with optimized performance. *Adv. Opt. Mater.* **6**, 1800213.
 36. Xu, X., Li, S., Chen, J., Cai, S., Long, Z., and Fang, X. (2018). Design principles and material engineering of ZnS for optoelectronic devices and catalysis. *Adv. Funct. Mater.* **28**, 1802029.
 37. Barman, B., Banger, K.V., and Shivakumar, G. (2019). Preparation of thermally deposited $\text{Cu}_x(\text{ZnS})_{1-x}$ thin films for opto-electronic devices. *J. Alloys Compd.* **772**, 532–536.
 38. Welch, A.W., Zawadzki, P.P., Lany, S., Wolden, C.A., and Zakutayev, A. (2015). Self-regulated growth and tunable properties of CuSbS_2 solar absorbers. *Sol. Energy Mater. Sol. Cells* **132**, 499–506.
 39. Baranowski, L.L., Zawadzki, P., Christensen, S., Nordlund, D., Lany, S., Tamboli, A.C., Gedvilas, L., Ginley, D.S., Tumas, W., Toberer, E.S., et al. (2014). Control of doping in Cu_2SnS_3 through defects and alloying. *Chem. Mater.* **26**, 4951–4959.
 40. Jain, A., Ong, S.P., Hautier, G., Chen, W., Richards, W.D., Dacek, S., Cholia, S., Gunter, D., Skinner, D., Ceder, G., and Persson, K.A. (2013). The materials project: A materials genome approach to accelerating materials innovation. *APL Mater.* **1**, 011002.
 41. Madsen, G.K., and Singh, D.J. (2006). BoltzTraP. A code for calculating band-structure dependent quantities. *Comput. Phys. Commun.* **175**, 67–71.
 42. Ricci, F., Chen, W., Aydemir, U., Snyder, G.J., Rignanes, G.-M., Jain, A., and Hautier, G. (2017). An ab initio electronic transport database for inorganic materials. *Sci. Data* **4**, 170085.
 43. Smilgies, D.-M. (2009). Scherrer grain-size analysis adapted to grazing-incidence scattering with area detectors. *J. of Appl. Crystallogr.* **42**, 1030–1034.
 44. Thornton, J.A. (1977). High rate thick film growth. *Annu. Rev. Mater. Sci.* **7**, 239–260.

45. Honig, R.E. (1958). Sputtering of surfaces by positive ion beams of low energy. *J. of Appl. Phys.* 29, 549–555.
46. Tauc, J., and Menth, A. (1972). States in the gap. *J. Non-Cryst. Solids* 8, 569–585.
47. Urbach, F. (1953). The long-wavelength edge of photographic sensitivity and of the electronic absorption of solids. *Phys. Rev.* 92, 1324.
48. Fan, H. (1956). Infra-red absorption in semiconductors. *Rep. Prog. Phys.* 19, 107.
49. Werner, F. (2017). Hall measurements on low-mobility thin films. *J. Appl. Phys.* 122, 135306.
50. Haacke, G. (1976). New figure of merit for transparent conductors. *J. Appl. Phys.* 47, 4086–4089.
51. Mendez-Gamboa, J., Castro-Rodriguez, R., Perez-Quintana, I., Medina-Esquivel, R., and Martel-Arbelo, A. (2016). A figure of merit to evaluate transparent conductor oxides for solar cells using photonic flux density. *Thin Solid Films* 599, 14–18.
52. Hoshina, T., and Kawai, H. (1980). Luminescence excitation spectra and their exciton structures of ZnS phosphors. I. Mn, (Cu, Al), (Ag, Al) and (Au, Al) doped phosphors. *Jpn. J. Appl. Phys.* 19, 267.
53. Pham, H.H., Barkema, G.T., and Wang, L.-W. (2015). DFT+U studies of Cu doping and p-type compensation in crystalline and amorphous ZnS. *Phys. Chem. Chem. Phys.* 17, 26270–26276.
54. Kumar, M., Dubey, A., Adhikari, N., Venkatesan, S., and Qiao, Q. (2015). Strategic review of secondary phases, defects and defect-complexes in kesterite CZTS-Se solar cells. *Energy Environ. Sci.* 8, 3134–3159.
55. Siol, S., Holder, A., Steffes, J., Schelhas, L.T., Stone, K.H., Garten, L., Perkins, J.D., Parilla, P.A., Toney, M.F., Huey, B.D., et al. (2018). Negative-pressure polymorphs made by heterostructural alloying. *Sci. Adv.* 4, eaaq1442.
56. Xiang, H., Wei, S.-H., Chen, S., and Gong, X. (2009). Ordered ground state wurtzite alloys from zinc-blende parent compounds. *Phys. Rev. B* 80, 113201.
57. Han, Y., Holder, A.M., Siol, S., Lany, S., Zhang, Q., and Zakutayev, A. (2018). Zinc-stabilized manganese telluride with wurtzite crystal structure. *J. Phys. Chem. C* 122, 18769–18775.
58. Glas, F., Harmand, J.-C., and Patriarche, G. (2007). Why does wurtzite form in nanowires of III-V zinc blende semiconductors? *Phys. Rev. Lett.* 99, 146101.
59. Allen, E.T., Crenshaw, J.L., and Merwin, H.E. (1912). The sulphides of zinc, cadmium, and mercury; their crystalline forms and genetic conditions; microscopic study by H.E. Merwin. *Am. J. Sci.* 202, 341–396.
60. Piper, W., and Polich, S. (1961). Vapor-phase growth of single crystals of II-VI compounds. *J. Appl. Phys.* 32, 1278–1279.
61. Qadri, S., Skelton, E., Hsu, D., Dinsmore, A., Yang, J., Gray, H., and Ratna, B. (1999). Size-induced transition-temperature reduction in nanoparticles of ZnS. *Phys. Rev. B* 60, 9191.
62. Lorenz, C.D., and Ziff, R.M. (1998). Precise determination of the bond percolation thresholds and finite-size scaling corrections for the sc, fcc, and bcc lattices. *Phys. Rev. E* 57, 230.
63. Cantor, B., and Cahn, R. (1976). Metastable alloy phases by co-sputtering. *Acta Metall.* 24, 845–852.
64. Holder, A.M., Siol, S., Ndione, P.F., Peng, H., Deml, A.M., Matthews, B.E., Schelhas, L.T., Toney, M.F., Gordon, R.G., Tumas, W., et al. (2017). Novel phase diagram behavior and materials design in heterostructural semiconductor alloys. *Sci. Adv.* 3, e1700270.
65. Öztas, M., Bedir, M., Yazici, A.N., Kafadar, E.V., and Toktamış, H. (2006). Characterization of copper-doped sprayed ZnS thin films. *Phys. B Condens. Matter* 381, 40–46.
66. Mohamed, S.H. (2010). Photocatalytic, optical and electrical properties of copper-doped zinc sulfide thin films. *J. Phys. D Appl. Phys.* 43, 035406.
67. Jose, E., and Kumar, M.S. (2017). Room temperature deposition of highly crystalline Cu-Zn-S thin films for solar cell applications using SILAR method. *J. Alloys Compd.* 712, 649–656.
68. Duncan, K.S., Taylor, J.D., Jonak, M., Derricutt, K.O., Tallon, A.G., Wilshaw, C.E., Smith, J.A., and Fox, N.A. (2017). Characterisation of p-type ZnS: Cu transparent conducting films fabricated by high-temperature pulsed laser deposition. *arXiv*, arXiv:1711.07579.
69. Mallick, A., Chattopadhyay, S., De, G., and Basak, D. (2019). High figure of merit p-type transparent conducting thin film based on solution processed CuS-ZnS nanocomposite. *J. Alloys Compd.* 770, 813–822.
70. Yildirim, M.A., Ateş, A., and Astam, A. (2009). Annealing and light effect on structural, optical and electrical properties of CuS, CuZnS and ZnS thin films grown by the SILAR method. *Phys. E Low Dimens. Syst. Nanostruct.* 41, 1365–1372.
71. Dula, M., Yang, K., and Ichimura, M. (2012). Photochemical deposition of a p-type transparent alloy semiconductor ($\text{Cu}_x\text{Zn}_y\text{S}$). *Semicond. Sci. Technol.* 27, 125007.
72. Yang, K., Nakashima, Y., and Ichimura, M. (2012). Electrochemical deposition of $\{\text{Cu}_x\text{S}\}$ and $\{\text{Cu}_x\text{Zn}_y\text{S}\}$ thin films with p-type conduction and photosensitivity. *J. Electrochem. Soc.* 159, H250–H254.
73. Michael, R.J.V., Theerthagiri, J., Madhavan, J., Umopathy, M.J., and Manoharan, P.T. (2015). Cu_2S -incorporated ZnS nanocomposites for photocatalytic hydrogen evolution. *RSC Adv.* 5, 30175–30186.
74. Ortiz-Ramos, D.E., González, L.A., and Ramirez-Bon, R. (2014). p-Type transparent Cu doped ZnS thin films by the chemical bath deposition method. *Mater. Lett.* 124, 267–270.
75. Ichimura, M., and Maeda, Y. (2015). Conduction type of nonstoichiometric alloy semiconductor $\text{Cu}_x\text{Zn}_y\text{S}$ deposited by the photochemical deposition method. *Thin Solid Films* 594, 277–281.
76. Fernando, W., Jayathillekea, K., Wijesundera, R., and Siripala, W. (2016). Growth of CuZnS Thin Films by Sequential Electrodeposition and Sulphurisation (Faculty of Science, University of Kelaniya).
77. Tong, B., and Ichimura, M. (2016). Annealing of p-type wide-gap $\{\text{Cu}_x\text{Zn}_y\text{S}\}$ thin films deposited by the photochemical deposition method. *Jpn. J. Appl. Phys.* 55, 098004.
78. Shimose, H., Singh, M., Ahuja, D., Zhao, W., Shan, S., Nishino, S., Miyata, M., Higashimine, K., Mott, D., Koyano, M., et al. (2016). Copper sulfide-zinc sulfide janus nanoparticles and their Seebeck characteristics for sustainable thermoelectric materials. *J. Phys. Chem. C* 120, 5869–5875.
79. Rauf, I. (1996). Structure and properties of tin-doped indium oxide thin films prepared by reactive electron-beam evaporation with a zone-confining arrangement. *J. of Appl. Phys.* 79, 4057–4065.
80. Nagarajan, R., Draeseke, A., Sleight, A., and Tate, J. (2001). p-type conductivity in $\text{CuCr}_{1-x}\text{Mg}_x\text{O}_2$ films and powders. *J. Appl. Phys.* 89, 8022–8025.
81. Mattox, D.M. (2010). Handbook of Physical Vapor Deposition (PVD) Processing (William Andrew).
82. Lowndes, D.H., Geohagan, D., Poretzky, A., Norton, D., and Rouleau, C. (1996). Synthesis of novel thin-film materials by pulsed laser deposition. *Science* 273, 898–903.
83. Michaelsen, C., Barmak, K., and Weihs, T. (1997). Investigating the thermodynamics and kinetics of thin film reactions by differential scanning calorimetry. *J. Phys. D Appl. Phys.* 30, 3167.
84. Green, M.L., Takeuchi, I., and Hatrick-Simpers, J.R. (2013). Applications of high throughput (combinatorial) methodologies to electronic, magnetic, optical, and energy-related materials. *J. Appl. Phys.* 113, 231101.
85. Talley, K.R., Bauers, S.R., Melamed, C.L., Papac, M.C., Heinselman, K.N., Khan, I., Roberts, D.M., Jacobson, V., Mis, A., Brennecke, G.L., et al. (2019). COMBIgor: data analysis package for combinatorial materials science. *ACS Comb. Sci.* <https://doi.org/10.1021/acscombsci.9b00077>.
86. Zakutayev, A., Wunder, N., Schwarting, M., Perkins, J.D., White, R., Munch, K., Tumas, W., and Phillips, C. (2018). An open experimental database for exploring inorganic materials. *Sci. Data* 5, 180053.
87. Giannuzzi, L.A., and Stevie, F.A. (1999). A review of focused ion beam milling techniques for TEM specimen preparation. *Micron* 30, 197–204.
88. Mayer, M. (1997). SIMNRA User's Guide (Max-Planck-Institut für Plasmaphysik Garching).